

Video-based observations of nearshore sand ripples and ripple migration

J. M. Becker,¹ Y. L. Firing,² J. Aucan,² R. Holman,³ M. Merrifield,² and G. Pawlak⁴

Received 21 December 2005; revised 3 August 2006; accepted 8 September 2006; published 25 January 2007.

[1] Observations of $O(1\text{ m})$ length and $O(0.1\text{ m})$ height sand ripples at Waimea Bay, a steep (slope ~ 0.05) pocket beach on the north shore of Oahu, Hawaii, are presented. Time series of ripple patterns over a 900 m^2 section of the nearshore in depths of 1–2 m are obtained using time-averaged video images from an Argus station overlooking the bay. Ripples are detected during weak wave conditions in the summer or between winter swell events. The ripple field exhibits narrow-band wave number structure, with ripple crests oriented parallel to the shoreline. The ripple wavelengths vary with wave orbital displacements, but they are shorter than predicted by orbital vortex ripple scaling relationships. A new suspension-limited model (Smith and Wiberg, 2006; Traykovski, 2006) in which the suborbital ripple wavelengths vary with wave period appears to describe well the observed ripple wavelength scaling. Lagged correlations between sequential Argus images reveal area-average ripple migration rates ranging from -3.3 m day^{-1} (offshore) to 4.5 m day^{-1} . The corresponding estimated sediment transport ranges from $-0.3\text{ m}^3\text{ m}^{-1}\text{ day}^{-1}$ to $0.5\text{ m}^3\text{ m}^{-1}\text{ day}^{-1}$, similar to previous estimates of cross-shore transport based on observed volume changes at the subaerial beach. This suggests that the recovery of beach sand following major swell-driven erosion events may be accomplished in part by the shoreward migration of seabed ripples.

Citation: Becker, J. M., Y. L. Firing, J. Aucan, R. Holman, M. Merrifield, and G. Pawlak (2007), Video-based observations of nearshore sand ripples and ripple migration, *J. Geophys. Res.*, 112, C01007, doi:10.1029/2005JC003451.

1. Introduction

[2] Seabed ripples have been the focus of a variety of observational and theoretical studies in part due to their impact on sediment transport. Sand ripples are an important source of hydrodynamic roughness [Ardhuin *et al.*, 2002] for the nearshore flows that drive sediment transport, and ripple migration may contribute directly to sediment transport [e.g., Traykovski *et al.*, 1999; Amos *et al.*, 1999; Hanes *et al.*, 2001; Crawford and Hay, 2001; Williams and Rose, 2001]. Seabed ripple spacings that scale with wave orbital diameter are classified as orbital ripples, those that scale with sand grain diameter are classified as anorbital ripples, and those with spacings that lie between the orbital and anorbital scalings are classified as suborbital ripples [e.g., Clifton and Dinger, 1984; Wiberg and Harris, 1994]. The dynamics of ripple formation and evolution as a function of hydrodynamic forcing remains an active field of study.

[3] Ripple characteristics in the nearshore have been measured in water depths $\leq 11\text{ m}$ using a variety of techniques (see Table 1 for a summary of recent field studies). Traykovski *et al.* [1999] used a rotary sidescan sonar to image bedform geometry and migration over a 35 m^2 area at LEO-15, the Long Term Ecosystem Observatory off the coast of southern New Jersey. During the 2 week experiment, six tropical storms passed to the east of their study site, resulting in approximately 1 m significant wave heights. Various ripple types were observed, including three-dimensional short crested ripples that occurred during the transitional stage at the beginning of a storm event, and two-dimensional vortex ripples, the predominant pattern during their experiment. They demonstrated that the wavelength, λ , of the two-dimensional vortex ripples scaled with the significant wave orbital diameter, $d_{0.13}$, according to $\lambda = 0.75d_{0.13}$. They observed ripples as large as 1 m wavelength and 0.15 m amplitude.

[4] Hanes *et al.* [2001] used an acoustic multiple transducer array to measure sand ripples off the coast of Duck, North Carolina. They classified their observations as short ($0.04\text{ m} < \lambda < 0.25\text{ m}$) and long wave ($0.35\text{ m} < \lambda < 2.40\text{ m}$) ripples. Short ripples were observed less frequently than long ripples because the short ripples tended to flatten and disappear during energetic wave conditions. The short ripple dimensions were consistent with anorbital ripple scalings and existing models [Neilsen, 1981; Wiberg and Harris, 1994]. In contrast, Hanes *et al.* [2001] found that existing models of orbital vortex ripples underpredicted the

¹Department of Geology and Geophysics, University of Hawaii at Manoa, Honolulu, Hawaii, USA.

²Department of Oceanography, University of Hawaii at Manoa, Honolulu, Hawaii, USA.

³College of Oceanic and Atmospheric Sciences, Oregon State University, Corvallis, Oregon, USA.

⁴Department of Ocean and Resources Engineering, University of Hawaii at Manoa, Honolulu, Hawaii, USA.

Table 1. Summary of Nearshore Ripple Studies^a

	Duck	Queensland	Martinique	LEO-15	Waimea
slope		0.035	0.001	0.002	0.05
D_{50} , mm	0.157–1.466	0.174	0.1	0.4	0.65
λ , m	0.04–2.40	0.08	0.07–0.24	0.10–1.00	0.4–1.2
Height, cm	0.3–6	0.3		4–15	~10–20
Rate, m day ⁻¹	8.6–10.8	-10.1–+4.3	±2.4	0.24 (mean)	-3.3–+4.5
h , m	1.4–6.8	3.5	10	11	1
T , s	3–16	4–10	4–11	5–16	5–18
H_{sig} , m	0.2–2.7	0.6–1	0.3–1.7	~1	0.2–1

^aBeach, ripple, and wave characteristics at Duck, North Carolina [Hanes *et al.*, 2001], Queensland, Nova Scotia [Crawford and Hay, 2001], Martinique, Nova Scotia [Boyd *et al.*, 1988], LEO-15, New Jersey [Traykovski *et al.*, 1999], and Waimea Bay, Hawaii [current work and Parker, 1987]. Columns are beach slope, median sand grain diameter D_{50} , ripple wavelength λ , ripple height, ripple migration rate (\mp corresponds to offshore/onshore migration), average water depth h , period of wave forcing T , and height of wave forcing H_{sig} . Wave conditions at the Waimea study site are estimated by SWAN from offshore buoy data.

length and overpredicted the height of the long wave ripples.

[5] In an earlier study, Boyd *et al.* [1988] used time-lapse underwater photography over a 0.46 m² area to identify six ripple types off Martinique Beach on the Atlantic coast of Nova Scotia, Canada during low to moderate energy summer wave conditions where significant wave heights reached 1.7 m. Two of the ripple types were equilibrium forms (short ($\lambda < 0.12$ m) and long ($\lambda > 0.16$ m) wavelength regular ripples) while the remaining four types were transitional bedforms that occurred when the ripple field was changing orientation or dimensions. The maximum observed ripple wave length in the Boyd *et al.* [1988] study was approximately 0.24 m.

[6] Crawford and Hay [2001] measured bedform evolution at Queensland Beach, Nova Scotia, using a laser-video bed profile imaging system and a rotary sidescan acoustic system during an autumn storm event. Four bed states were observed over the course of the storm event: irregular (relict) ripples evolved into cross ripples which were followed by linear transition ripples and flatbed conditions that occurred at the most energetic storm conditions. As the storm decayed, the bedforms transitioned from flatbed to linear transition ripples to cross ripples back to irregular ripples. The linear transition ripples were the focus of the Crawford and Hay [2001] study and were shown to be anorbital ripples with wavelengths ~0.08 m.

[7] In these field studies, the translation of ripples over time was observed. Crawford and Hay [2001] found that during storm growth, linear transition ripples migrated seaward with a maximum rate of 10.1 m day⁻¹ as Queensland Beach eroded, and shoreward with a maximum rate of 4.3 m day⁻¹ during the subsequent phase of storm decay as the beach accreted. The observed ripple migration rates were found to be highly correlated with nearbed wave orbital velocity skewness. Boyd *et al.* [1988] observed offshore and onshore migration of ripples with maximum rates of 2.4 m day⁻¹; onshore migration was most frequently observed during their 18-day experiment. Hanes *et al.* [2001] reported onshore migration of long (1.0–1.3 m) ripples over an 85 min time span at a rate equivalent to 8.6 m day⁻¹. Traykovski *et al.* [1999] observed onshore migration rates of up to 0.8 m day⁻¹ and used these rates to estimate the amplitude and direction of sediment transport due to ripple migration assuming that the volume of sand contained in the ripples is transported with the ripples.

Measurements of suspended load transport 6–80 cm above the bed could not account for the amplitude or direction of the transport; hence Traykovski *et al.* [1999] concluded that the ripple migration was associated with bedload or near-bottom suspended load transport and might be the dominant mode of cross-shore sediment transport at sites similar to LEO-15 with medium to coarse sand.

[8] In this study we examine ripple properties at Waimea Bay, Hawaii, a steep, pocket beach on the north shore of the island of Oahu. These observations complement previous field studies, in that Waimea Bay is a high-energy beach (winter swell heights frequently exceed 3 m) with significant cross-shore sediment transport (typically of order 0.1 m³ m⁻¹ day⁻¹, but as much as 4–6 m³ m⁻¹ day⁻¹ [Dail *et al.*, 2000]). Dail *et al.* [2000] document energetic winter swell events that quickly erode the beach (up to 3 m of beach elevation change in a day), followed by weaker wave conditions that lead to beach recovery over longer timescales (1 week). A motivation for the present study is to determine whether ripple migration might contribute to onshore sand transport, particularly during phases of beach accretion.

[9] Our method for detecting ripples differs from previous in situ studies in that we use the Argus system of video imaging to observe the sand bed from above the ocean surface. Argus stations have been established at a number of beaches around the world to monitor the spatiotemporal behavior of the nearshore [Holman *et al.*, 1993]. Inference of wave properties, currents, and sand movements have been obtained from Argus images using patterns that appear on the ocean surface. For example, sand bars can be located because waves preferentially break over shallow bars, creating zones of persistent white water that appear as bright pixel intensity in time-averaged images [Lippmann and Holman, 1993]. An alternative approach is that of Clarke and Werner [2003] who used adaptive filtering of video data to remove the surface white water signal, enabling the visualization of bedforms through the water column. Because of the clarity of the water at Waimea Bay, bedform patterns can be detected in time-average Argus images without special processing. These patterns include beach cusps, underwater “steps” (which generally follow the shoreline contour), small troughs and bars, and especially wave-generated sand ripples. These sand ripples are the most persistent and widespread features visible in the Argus images and are the focus of the present study.



Figure 1. Argus snapshot and 10-min time average from 23 March 2003, 0820 HST (year day 446).

[10] The paper is organized as follows. In section 2 we describe the Argus data set and image processing. In section 2.3 we describe how we obtain estimates of wave orbital diameters from offshore directional buoy data and numerical simulations of the wave transformations. We then compare in section 3.1 our results for ripple wavelengths with our estimates of wave orbital diameters and with the suspension-limited model of *Smith and Wiberg*, [2006] as

modified by *Traykovski* [2006]. In addition, in section 3.2 we obtain estimates of ripple migration and transport rates from the Argus images and compare the results with previous beach survey data [*Dail et al.*, 2000].

2. Data

2.1. Description

[11] The Waimea Bay Argus station was established in 1995 by the Coastal Imaging Laboratory (CIL) at Oregon State University. It is one of 14 CIL Argus stations currently in operation worldwide. The Waimea station consists of five cameras mounted in a church tower overlooking the bay from the northeast side. Four of the cameras provide a panoramic view from the shore to the open ocean while a fifth camera is focused on the midbeach foreshore on the eastern side of the bay. In this study we examine images from the fifth camera, an example of which is shown in Figure 1. A typical pixel footprint in the area we analyze here is 0.04 m^2 . Each hour, a single snapshot image and a 10-min time average are acquired from each camera using an on-site Unix SGI computer. The JPEG images are transmitted daily to CIL for further processing and archiving.

[12] Examples of a snapshot and 10-min time average of the beach at Waimea show rhythmic features that are aligned approximately parallel to the shore (Figure 1). The pattern is barely detectable in the snapshot but is clearly evident in the time average. Underwater photographs and visual observations of the ripple bed at Waimea Bay (Figure 2) confirm that the features in the Argus images are sand ripples. Between the shoreline and approximately 3 m water depth, the seabed ripples were mostly uniform in shape, nearly parallel and linear, with wider troughs than crests and a steeper cap on the crests. Although wave conditions were weak ($T \sim 10 \text{ s}$, offshore $H_{sig} \sim 1 \text{ m}$) at the time of the underwater observations described, sand bursting off the top of the ripple crests was observed when waves passed over in up to 2 m depth, suggesting that these are wave-formed ripples.

[13] We have inspected approximately 4000 time-averaged Argus images from 2002 to 2003. Ripples are observed at all times of the day (nominally between 0600 and 1700 HST), but they are most evident in the early morning (0800–1000) when local breezes tend to be light.



Figure 2. Underwater photos of seabed ripples at Waimea Bay, Hawaii, from June 2002.

Ripples are not generally visible during the early afternoon due to direct sun glint into the southwestward facing camera. Other factors that adversely affect the detection of ripples on the seabed include cloud cover which reduces the light level and wind or waves which cause bubbles and suspended sand in the water column. Under moderate to large swell conditions ($H_{sig} \geq 2$ m in the bay), the seabed generally is not visible. Thus our data can confirm the presence of ripples, but not their absence, for example as might occur under strong wave flows that induce sheet-flow conditions on the bed. We often can document ripple features before and after energetic swell events but not the transitional behavior of the ripple field during the events. In addition, the beach at Waimea serves as a dam for the Waimea stream for most of the year. During heavy rains or major beach erosion events, the beach gives way allowing the stream to flow into the ocean, creating a sizable sand spit. Images in which the sand spit is visible are not used in our analysis.

2.2. Image Processing

[14] *Clarke and Werner* [2003] use a varying brightness threshold to eliminate foam- or sediment-contaminated pixels in video images and then average the filtered images to produce the equivalent of a time exposure in which the bottom is visible while the changing surface is filtered out. They then transform their images to a plan view using a set of ground control points and correct for lens distortion and the effects of refraction.

[15] Because we lack high-frequency sampling in time, we do not apply their pixel brightness filtering. Instead we use the standard 10-min time averages to identify ripples. We find that this simple method produces clear images of the bottom (e.g., Figure 1) approximately 50% of the time during summer conditions (April through October) and 15% of the time during winter conditions when north swells are likely (November–March), with the rest being obscured by waves or by sun glint as described in §2.1 above.

[16] The transformation to plan view is performed using coordinates surveyed at system installation and software provided by the CIL [*Holland et al.*, 1997]. We transform the images to real (x, y) coordinates on the water surface, and then apply refraction corrections, following *Clarke and Werner* [2003],

$$\begin{aligned} d &= \sqrt{(x - x_c)^2 + (y - y_c)^2}, \\ \theta_a &= \tan^{-1} \left(\frac{d}{z_c} \right), \\ \theta_w &= \sin^{-1} \left(\frac{\sin \theta_a}{1.34} \right), \\ d_\rho &= (h + dh) \tan(\theta_w), \\ (x_n, y_n) &= \left(x + \frac{d_\rho}{d} (x - x_c), y + \frac{d_\rho}{d} (y - y_c) \right), \end{aligned} \quad (1)$$

where $(x, y, 0)$ is the position of the data point from the plan view program, (x_c, y_c, z_c) is the camera position, θ_a and θ_w are the angles of the ray to the vertical in air and water, respectively, 1.34 is the index of refraction for salt water, $h(x, y)$ is the mean water depth, and dh is the depth change due to the tide (the average tidal range at Waimea Bay is 0.5 m). The data are then interpolated from (x_n, y_n) back to

the regular (x, y) grid. We use an (x, y) grid with 0.1 m spacing. Bathymetric surveys during the Argus sampling period are not available. Instead the average bathymetry, $h(x, y)$, over the study area is estimated from the images as described in Appendix A. The resulting depth grid, ranging from 0.1 to 2.0 m in the analyzed area, is used to calculate the refraction correction according to (1).

2.3. Wave Observations and Model Simulations

[17] Offshore wave conditions are measured by a Datawell directional waverider buoy located at $21^\circ 40.3$ N, $158^\circ 06.9$ W, approximately 5 km from shore in 200 m water depth. The buoy provides directional spectral estimates at 30-min intervals. As we do not have continuous in situ wave measurements over the Argus image field, we use the SWAN (Simulating Waves Nearshore) model to simulate the wave transformation between the offshore buoy and Waimea Bay. SWAN is a third generation spectral wave model designed to predict waves in coastal environments [*Booij et al.*, 1999; *Ris et al.*, 1999]. It accounts for propagation through space and for refraction and shoaling due to variations in bottom depth. The model is initialized using daily averages of the offshore wave height, period, and direction measured at the buoy, including only wave energy in the directional range 270° to 25° east of true north, as Waimea Bay is sheltered from wave energy outside of this direction band. A 50 m horizontal grid resolution is used and bottom topography is specified using SHOALS Lidar and National Ocean Service sounding data. We do not include the contribution of local wind seas, which typically are weak within the sheltered bay. To reduce the computation time of the simulation, the wind growth and white capping terms are turned off in the model, as well as the quadruplet wave-wave interaction, which would lead to numerical instability in the absence of wind. We use the default JONSWAP semiempirical expression from *Hasselmann et al.* [1973] for the bottom friction dissipation. On the basis of previous unpublished wave modeling studies of wave decay over rough topography around the Hawaiian Islands, we chose a friction coefficient of 0.38, one order of magnitude larger than the typical value for swell conditions [*Booij et al.*, 1999]. We note that SWAN does not include either shoreline reflection or nonlinear transformation of waves entering shallow water, both potentially important processes at our study site.

[18] To validate the SWAN model run, we compare the model output with current meter observations made in 10 m water depth near the center of the bay during a 17-day deployment in November–December 2004, and in 2.6 m water depth during a half-hour deployment in April 2006. At 10 m depth, the modeled and observed u_{rms} time series, taken ~ 0.7 m above the bottom, are significantly correlated ($R = 0.81$) and of the same amplitude. These comparisons were made for significant wave heights ranging from 0.2 to 1.5 m (computed over 1 hour record lengths from pressure measurements in 10 m; buoy significant wave heights ranged from 0.4 to 2.2 m). The measurements in 2.6 m depth were taken when $H_{sig} \sim 0.4$ m (buoy $H_{sig} = 0.7$ m) and the modeled and observed u_{rms} , measured ~ 0.6 m above the bottom, were likewise very similar in amplitude. On the basis of these comparisons, we believe that the SWAN simulations provide an accurate estimate of u_{rms} at

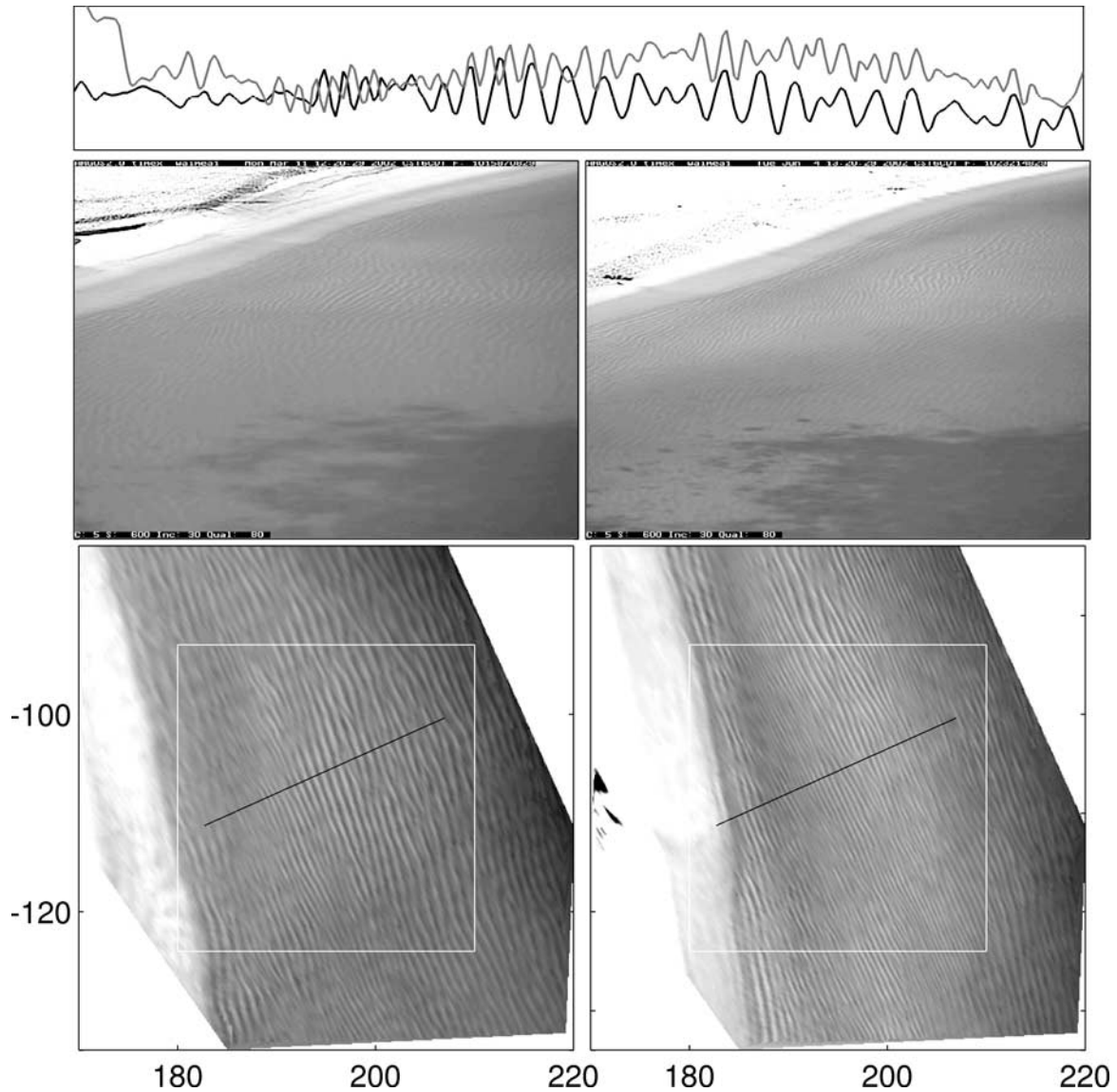


Figure 3. Original time average images (middle) and portion of plan view images (bottom) with box surrounding the subsection used in analysis. Left panels are from 11 March 2002, 0820 HST (year day 69), and right panels are from 4 June 2002, 0820 HST (year day 154). Also included (top) is intensity along the transect shown in the bottom panels, for 11 March (black line) and 4 June (gray).

our study site. For comparison with the ripple data, we use u_{rms} at a grid point in 1.3 m water depth near the center of our image area to compute wave orbital displacements according to

$$d_{0/3} = \frac{4u_{rms}T}{2\pi}, \quad (2)$$

where T is the dominant buoy period input to SWAN. A comparison of wave orbital diameter in 2.6 m calculated from SWAN by (2), $d_{0/3} = 3.7$ m, and calculated directly from the current record following *Hanes et al.* [2001], $d_{0/3} = 4.0$ m, demonstrates that SWAN estimates of orbital diameter are consistent with directly measured values in shallow water and weak wave conditions ($H_{sig} = 0.4$ m). Thus while we could not validate the SWAN predictions in the 1–2 m water depths of our study site for the full range

of incident wave conditions, we find that (2) used with SWAN appears to give reasonable estimates of wave currents and orbital diameters near our study site.

3. Results

3.1. Ripple Wavelengths

[19] To obtain an estimate of the ripple wavelength from the Argus images, two-dimensional Fast Fourier Transforms (FFTs) are performed on a Hanning-windowed subsection of the transformed images (Figure 3). After smoothing, the wave number (k_x, k_y) is converted to polar coordinates (k, ϕ). We find that the temporal standard deviation of the angle of the spectral maximum, ϕ_p , is 2° and that ϕ_p shows no relationship to offshore wave direction, consistent with the shore-normal approach of the wave field and the shore-parallel orientation of the ripple field.

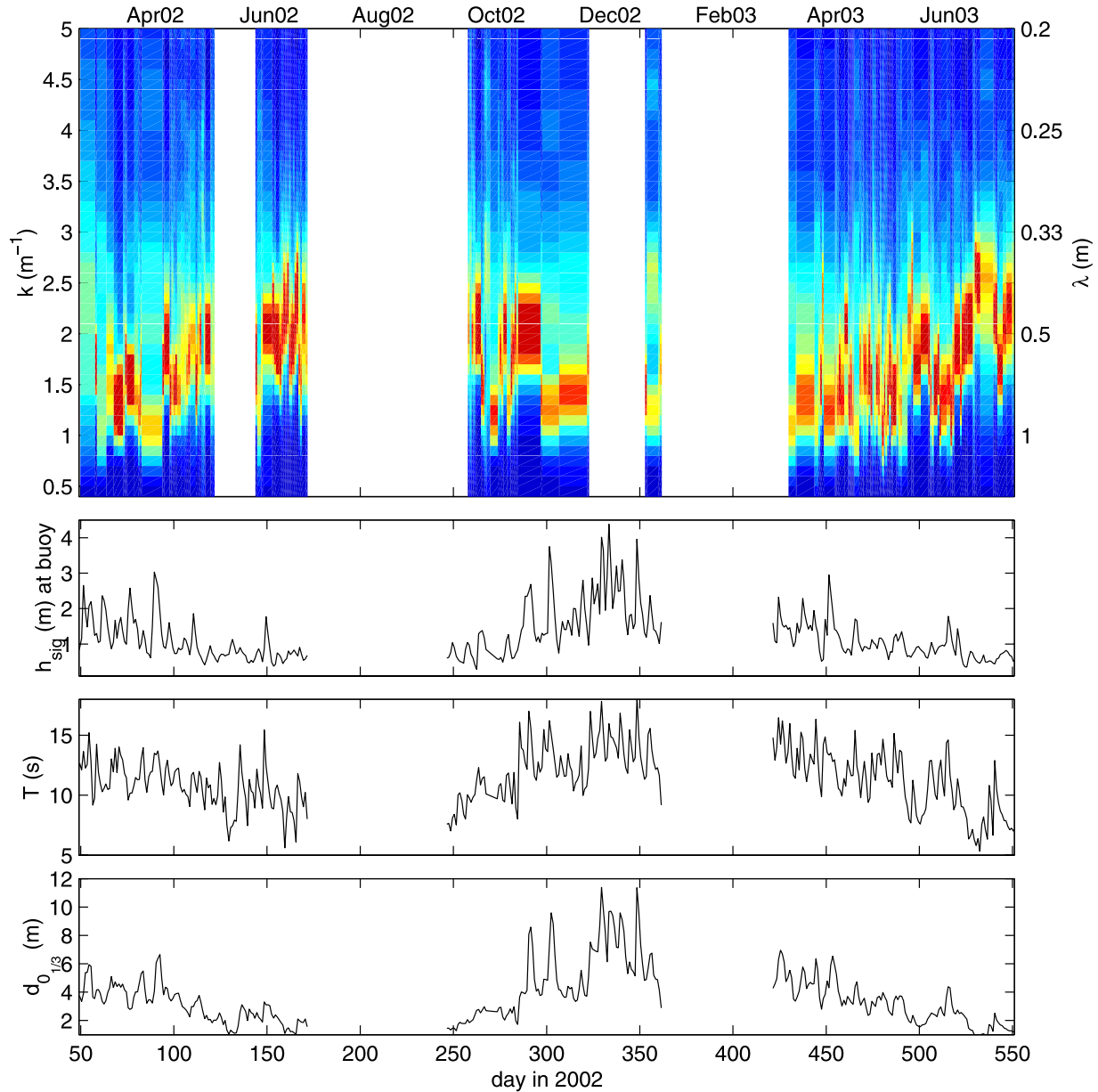


Figure 4. (top) Comparison of ripple wavelength (red denotes the most energetic wavelengths and blue the least), (second) offshore significant wave height from the window between 270° and 25° relative to true north, (third) peak wave period, and wave orbital diameter calculated from (2) in 1.3 m. All decrease from winter to summer (about day 90 to day 170 and day 455 to day 550).

[20] The ripple wavelength ($\lambda = \frac{2\pi}{k}$) spectra are obtained by averaging the wave number spectra with respect to ϕ (Figure 4). Gaps in the wavelength time series correspond to those periods when either the seabed was not visible in the Argus images or when the Argus station was not operational (e.g., from 22 June to 26 August 2002 (year days 172–237). Images from 27 August to 15 September 2002 (year days 238–257) had poor seabed visibility). Also plotted in Figure 4 are the significant wave height and dominant period from the offshore buoy and our estimate of $d_{0,1/3}$ in 1.3 m from SWAN u_{rms} and (2). Over time periods of weeks to months, ripple wavelengths appear to correspond to wave size and period, with wavelengths decreasing through spring into summer (i.e., year days 90–170 and 455–550).

[21] To obtain the data shown in Figure 4, the images that most clearly show the ripple field each day are selected and the wave number spectrum is estimated as described above. We find at least one clear image on 153 days during the study period. In addition, on 39, 10, and 1 of the 153 days we obtain 2, 3, and 4 wave number spectral estimates, respectively.

[22] For a time series of ripple wavelength, we use λ_p , the wavelength of the spectral peak, as a representative wavelength estimate. It is difficult to assign an uncertainty to λ_p , as the spectral peak may vary over the course of a day either due to actual changes in ripple wavelength caused by varying hydrodynamic conditions or due to spectral estimation errors that result from variable image quality. On the

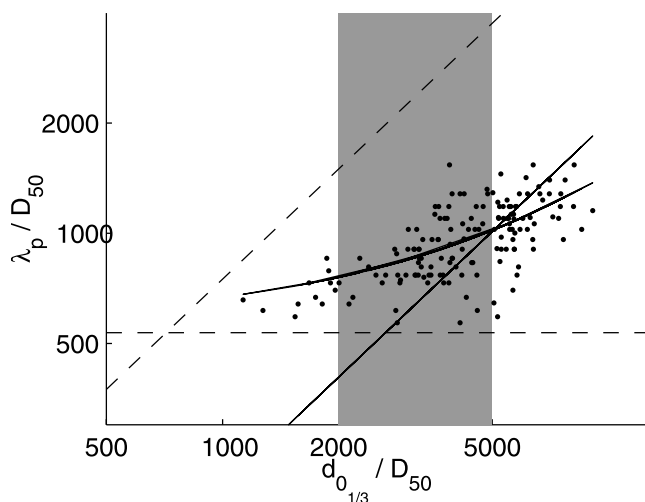


Figure 5. Ripple wavelength, λ_p , versus significant wave orbital diameter, $d_{0,1/3}$, both scaled by median grain size D_{50} . The dashed sloping line ($\lambda = 0.75d_{0,1/3}$) indicates the relationship for orbital ripples, the dashed horizontal line ($\lambda = 535D_{50}$) that for anorbital ripples, and the shaded area indicates the suborbital region [Traykovski *et al.*, 1999]. The solid curved line is the best fit to the data, $0.09d_{0,1/3} + 0.38$, and the solid straight line is $0.20 d_{0,1/3}$.

days on which we have more than one spectral estimate available, we obtain multiple (up to four) estimates of λ_p and average those values to obtain a mean daily wavelength. We choose to use only the clearest images each day in order to minimize errors in estimating λ_p resulting from poor image quality.

[23] We begin our examination of the relationship between sand ripples and waves at our site by calculating the Shields parameter, following Traykovski *et al.* [1999]:

$$\theta = \frac{1}{2} f_{2.5} \frac{u_{1/3}^2}{(s-1)gD_{50}} \quad (3)$$

where g is the acceleration due to gravity, D_{50} is the median grain diameter, $s = 2.6$ is the specific gravity of the calcareous sand [Smith and Cheung, 2003], $u_{1/3} = 2u_{rms}$ is the wave velocity corresponding to significant wave height and

$$f_{2.5} = \exp\left(5.213 \left[\frac{2.5D_{50}}{d_{0,1/3}/2}\right]^{0.194} - 5.977\right)$$

is Swart's formula for the wave friction factor [Swart, 1974; Neilsen, 1981]. Using the SWAN model results for 1.3 m depth, we find that $0.13 < \theta < 0.88$. We estimate the critical Shields parameter for this site to be ~ 0.04 using results for calcareous sand [Smith and Cheung, 2004]. That the Shields parameter is always above this critical value for the initiation of motion indicates that the ripple field at our study site is active and not composed of relict ripples. This is consistent with visual observations made by divers of sand bursting off the crests of the ripples during weak wave conditions (wave heights < 0.5 m).

[24] We next compare our estimate of the significant wave orbital diameter $d_{0,1/3}$, calculated by (2) using the SWAN model velocities as described above, with the ripple wavelength λ_p . Figure 5 shows λ_p/D_{50} versus $d_{0,1/3}/D_{50}$. Following Traykovski *et al.* [1999], we indicate the orbital (sloping dashed line, $\lambda = 0.75d_{0,1/3}$), suborbital (shaded region), and anorbital (horizontal dashed line, $\lambda = 535D_{50}$) regimes. In contrast to their observations and those of Clifton and Dingler [1984] and Wiberg and Harris [1994], our data do not appear to follow either the orbital or the anorbital scaling.

[25] Our data fall into the suborbital range but exhibit a positive linear trend, with a best fit line with slope 0.09 ± 0.02 (95% confidence interval), y-intercept $(0.38 \pm 0.05)/D_{50}$, and coefficient of determination $R^2 = 0.40$. For orbital ripples, it may be argued that at zero wave orbital diameter, the ripple wavelength should be zero as well; hence we also fit our data to a line through the origin and find the best fit has slope 0.20 ± 0.01 . As is apparent in Figure 5, the line with nonzero intercept fits the data better: the sum of the squares of the residuals is a factor of two less with the intercept than without it.

[26] The observed linear relationship between λ_p and $d_{0,1/3}$ suggests that the wavelength of the Waimea ripples is actively influenced by the wave forcing, as is the case with orbital ripples. The slope of our data (0.09 with a y-intercept or 0.20 without), however, is considerably smaller than previously reported values for orbital ripples (e.g., 0.65 from Clifton and Dingler [1984] and Wiberg and Harris [1994]; 0.75 from Traykovski *et al.* [1999]; 0.48 to 0.76 from Arduin *et al.* [2002]), which all appear to be obtained by fitting with zero y-intercept. That the Waimea ripple wavelengths are short compared to the scaling law for orbital ripples observed in other study areas and largely fall into the suborbital range (Figure 5) suggests that the ripple wavelength may be set by a combination of the wave orbital diameter and other parameters, such as grain size.

[27] In the field study of Traykovski *et al.* [1999], the maximum ripple wavelength observed was 100 cm. Traykovski *et al.* [1999] hypothesized that this wavelength marked the transition from orbital to suborbital ripples, the point at which a subsequent increase in wave orbital diameter does not lead to an increase in ripple wavelength. They found that existing models [e.g., Wiberg and Harris, 1994; Miller and Komar, 1980] underpredicted the maximum wavelength at the orbital-suborbital transition by a factor of 1.5–2.

[28] Recently, Smith and Wiberg [2006] have proposed a maximum orbital ripple wavelength that is determined by a suspension threshold based on a criterion of $u^*/w_s \sim 1$, where u^* is the grain roughness wave shear velocity and w_s is the sediment settling velocity. Traykovski [2006] suggests modifying this threshold to one based on the ratio of u_{rms}/w_s to avoid the introduction of a friction factor in the criterion for the maximum orbital ripple wavelength and the transition to the suborbital regime. Traykovski's [2006] model of ripple wavelength at the orbital-suborbital transition has

$$\begin{aligned} \lambda_t &= 0.75d_{0,1/3} = 3 \frac{u_{rms}}{\omega}, & u_{rms} &\leq \gamma w_s \\ \lambda_t &= 3 \frac{\gamma w_s}{\omega}, & u_{rms} &> \gamma w_s, \end{aligned} \quad (4)$$

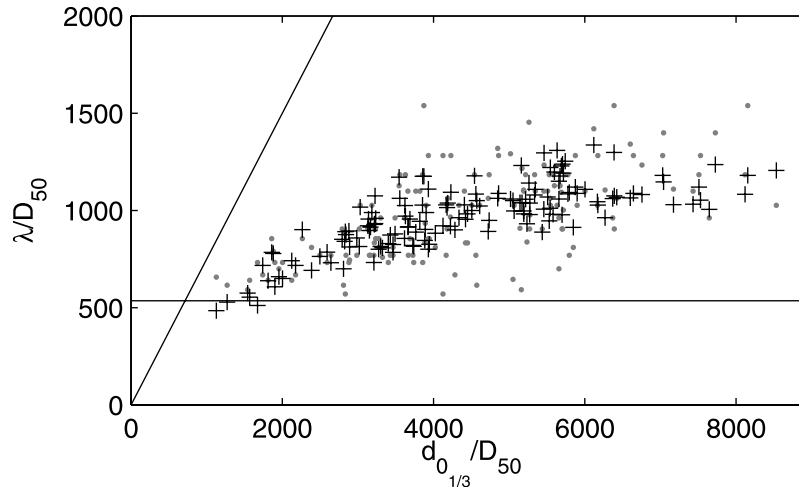


Figure 6. Suspension-limited ripple wavelength λ_t (pluses) from (4) with $w_s = 0.08$ m/s and $\gamma = 1.55$ and λ_p (dots) from Argus, both scaled by median grain size D_{50} . The correlation coefficient between λ_p and λ_t is 0.67. The solid sloping line, $\lambda = 0.75d_{0/1/3}$, indicates the orbital ripple scaling, and the solid horizontal line, $\lambda = 535D_{50}$, indicates the anorbital ripple scaling.

where $\omega = 2\pi/T$. Equation (4) may be understood by the following scaling argument. We define a sediment settling time scale T_s by assuming that the height above the bed at which the sediment is suspended is proportional to ripple height ζ , hence $T_s \propto \zeta/w_s$, where w_s is the sediment settling velocity. Relating ripple height to wavelength according to $\zeta = m\lambda/2$, where m is the ripple slope, assumed constant, we find $T_s \propto m\lambda/w_s$. Suborbital ripples occur when the settling time is the same scale as the wave period, $T_s \sim T$, and hence scale according to $\lambda_t \propto w_s T/m$. Defining γ as a constant proportional to $1/m$ (from ripple observations at LEO 15 and the Martha's Vineyard Coastal Observatory (MVCO), Traykovski [2006] found $\gamma = 2.1 \approx 1/(2m)$ for ripples with slopes of $m = 0.2-0.3$), we obtain the second of (4), $\lambda_t = 3\gamma w_s/\omega$. In the orbital regime, $\lambda_t = 0.75d_{0/1/3} = 3u_{rms}/\omega$, so that by assuming continuous wavelengths at the orbital-suborbital transition we obtain the threshold condition of (4), $u_{rms} = \gamma w_s$. Suborbital ripples have smaller wavelengths for a given wave orbital diameter than their orbital counterparts and are observed when the effects of suspended sediment become important, that is when the ratio of the sediment settling velocity to the horizontal fluid velocity is small relative to the ripple slope ($w_s/u_{rms} < 1/\gamma \propto m$). For ripple wavelengths larger than λ_p , (4), the settling timescale, T_s , would exceed the wave period, T . At these scales, suspension would exceed deposition and a stable bed would not be possible.

[29] We estimate from Smith and Cheung [2003] that $w_s = 0.08$ m/s for the calcareous sand of Waimea Bay. A regression analysis of λ_p and T gives $\gamma = 1.55$, which places all of our wavelength estimates in the suborbital regime (i.e., $u_{rms} > \gamma w_s$). By analogy with $\gamma \approx 1/(2m) = 2.1$ and $m = 0.2-0.3$ of Traykovski et al. [2006], ripple slopes of $m = 0.3-0.4$ are implied for our site. For the wavelengths observed, this slope range corresponds to ripple heights of 6–20 cm, which are consistent with observations by divers in this area (Table 1). We calculate λ_t from (4) using these values for w_s and γ and find that the correlation coefficient between λ_p and λ_t is $R = 0.67$ (Figure 6), better than the

correlation between λ_p and $d_{0/1/3}$ ($R = 0.63$, see above). In addition, in Figure 7 we present a time series of ripple wavelengths observed, λ_p , and predicted by (4), λ_t , and find that the correlation between the 7-day smoothed λ_p and λ_t is 0.85. We emphasize that in addition to fitting the observations better, the new suspension-limited model developed by Smith and Wiberg [2006] and modified by Traykovski [2006] provides a physical mechanism for the wavelength scaling of our suborbital ripple observations which was not provided by the straight line with intercept fit above.

3.2. Ripple Migration

[30] We first illustrate the nature of ripple migration in the image data using cross-shore transects (indicated by the black lines in Figure 3) from two representative days (Figure 8). Images collected on 27 April 2002 (year day 116) show ripples with wavelengths of 0.8 m that shift approximately one quarter wavelength toward shore between 0820 and 0920 HST, corresponding to a shoreward ripple migration rate of ~ 4.8 m day⁻¹. At this time, wave periods were 9 s, H_{sig} from SWAN near our image area was 0.6 m, and u_{rms} was 0.6 m s⁻¹. While the ripple migration rate from the 27 April 2002 images appears to be similar across the transect, at other times the rate varies with cross-shore distance. For example, a year later, on 26 April 2003 (year day 480), the ripple wavelength along the transect was 1 to 1.2 m and shoreward ripple migration rates varied from ~ 2.4 m day⁻¹ at the offshore edge to ~ 14.4 m day⁻¹ closest to shore. For reference, the SWAN predictions of H_{sig} and u_{rms} were similar to the conditions on 27 April 2002; however, the peak wave period was longer, at 12.5 s, on 26 April 2003.

[31] The spatial coverage of Argus allows for cross-shore ripple migration rate estimates over a broad area (30 m by 30 m) of the nearshore. We rotate time-averaged image data to a cross-/along-shore coordinate system and form seven 4-m bins in the cross-shore with 0.1-m resolution within each bin. Lagged correlations in space are calculated for each bin using data from adjacent hours. The lag which

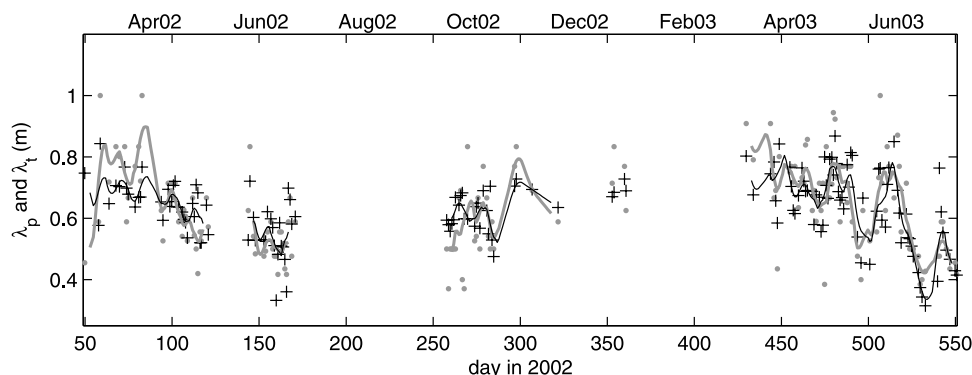


Figure 7. Ripple wavelength observed (dots and thick gray line) and predicted from the suspension threshold model (4) with $w_s = 0.08$ m/s and $\gamma = 1.55$ (pluses and thin black line). Lines are 7-day smoothed. The correlation between observed λ_p and modeled λ_t is 0.67 (unsmoothed) and 0.85 (smoothed).

produces maximum correlation is the ripple migration rate (distance moved in 1 hour) for that bin; only correlations greater than 0.7 are considered. Migration rates from 0820 to 0920 and from 0920 to 1020, the times of day when ripples are most easily detected, are averaged and smoothed over 1 m in the alongshore. We present in Figure 9 two examples of ripple velocity fields determined by this method. The ripple velocities on 26 April 2003 (Figure 9, left panel) are shoreward; however, speed varies across the image. If ripple migration were assumed to be indicative of sediment transport rates (see the discussion of this assumption, below), this cross-shore variation would suggest transport divergence, or a net loss of sand from the sample area. On 23 March 2002 (Figure 9, right panel), both onshore and

offshore migration are observed, with strong onshore rates close to shore and weaker offshore rates in the rest of the area. The scarcity of migration data points observed in this example is common on days with offshore migration.

[32] When ripple migration is detected, the propagation direction is predominantly onshore. From the 120 spatial points in the subgrid indicated by the white box in Figure 9 and from 151 sample days, significant migration rates were found for 53% of the total space/time points (53% had correlation >0.7). Of all the space/time points with significant migration rates, onshore migration occurs in 54% of cases, offshore migration in 16%, and zero migration (less than 5 cm displacement in an hour) in 29%. The dominance of onshore migration may be related to our sampling bias,

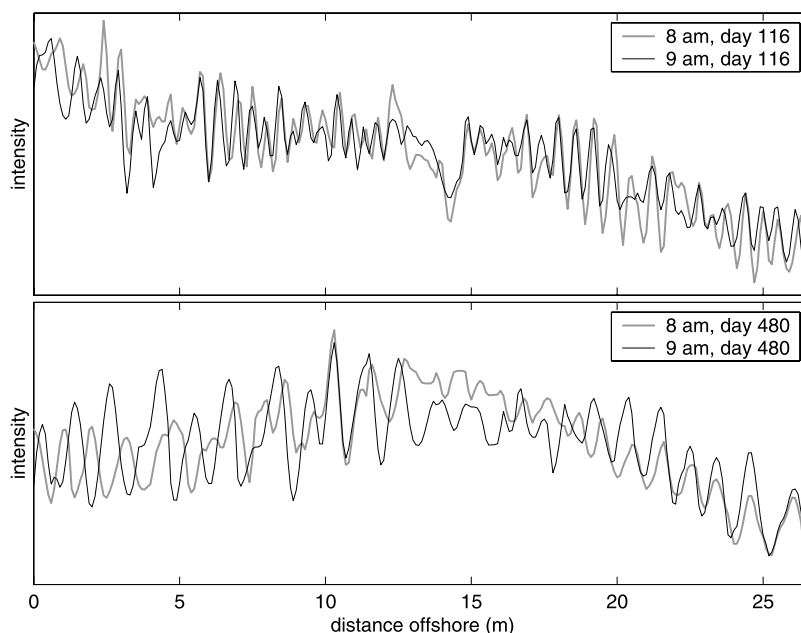


Figure 8. Ripple-normal cross-sections (black line in bottom panel of Figure 3) during low wave conditions (Trade wind swell ≤ 1 m) show ripple migration. The top panel shows shoreward migration at a rate of ~ 4.8 m day^{-1} on 27 April 2002 (year day 116). The bottom panel shows shoreward migration on 26 April 2003 (year day 480) at a rate varying from ~ 2.4 m day^{-1} in the offshore section to ~ 14.4 m day^{-1} in the onshore section, where there is a 180° phase change over the course of an hour.

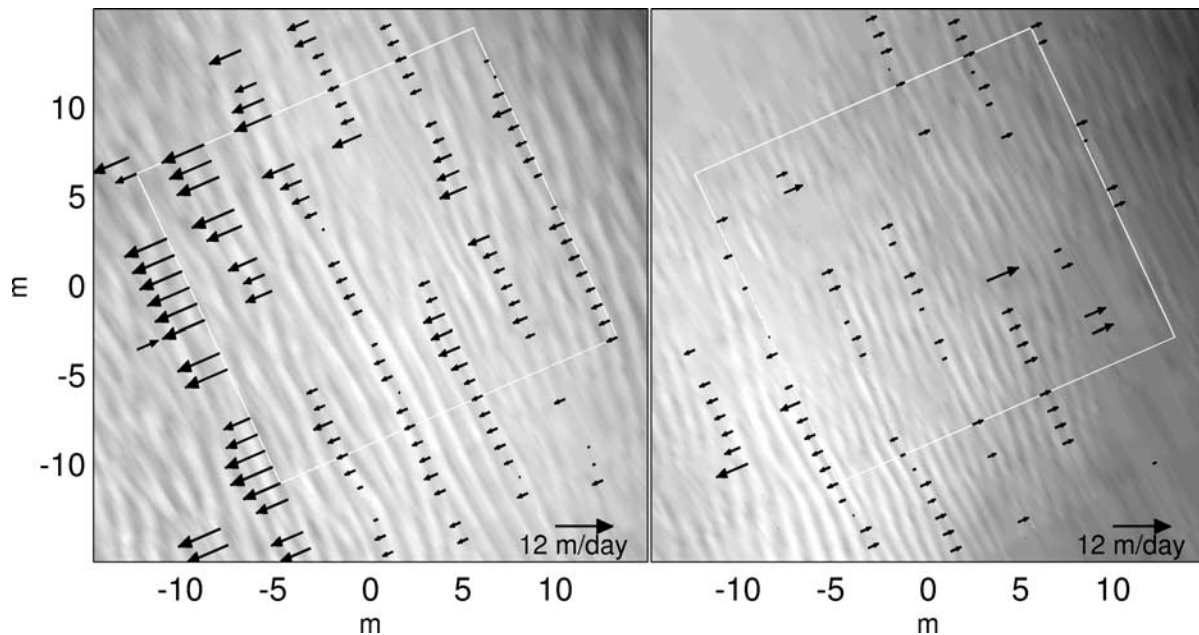


Figure 9. Ripple migration for 0820 to 0920 (HST), 26 April 2003 (year day 480, left) and 23 March 2002 (year day 81, right), superimposed on the 0920 images, showing onshore and offshore migration. The area delimited by the white box is used for calculating the averages presented in Figures 10 through 12.

discussed in section 2.2: in general, the small waves under which we can sample appear to drive onshore rather than offshore ripple migration.

[33] We characterize the temporal cross-shore variability of the migration rates in Figure 10 by time series of along-shore averaged rates for the six cross-shore lines in the subgrid (white box, Figure 9). We consider alongshore averages rather than rates at each grid point because of numerous data gaps in both space and time (e.g., Figure 9, right panel). Black (gray) bars in Figure 10 indicate migration rates for which more (fewer) than 40% of the along-shore points are available to contribute to the average. We find that the largest migration rates typically occur closest to shore and that, as described above, ripple migration is predominantly onshore. Spring–summer 2003 (1 April 2003 to 20 June 2003) has more strong onshore migration, with 14 days greater than one standard deviation from the mean, than spring–summer 2002 (1 April 2002 to 20 June 2002), which has only 5 such days. The wave conditions during the two periods were similar, suggesting that wave period and orbital velocity are good predictors of ripple wavelength but not of ripple migration rate. Antecedent beach conditions may play a role in the 2002–2003 difference.

[34] The predominance of onshore migration is evident in Figure 11, where we present histograms of along-shore averaged ripple migration rates at each of the six lines. It is also evident that more high rates are found close to shore than far from shore.

[35] We define the average migration rate in the subgrid (white box, Figure 9) as u_{ripple} and in Figure 12 present a comparison of u_{ripple} with the rms wave orbital velocity, u_{rms} , from the SWAN model. The sampling bias toward

smaller waves is evident in this figure. The area-averaged migration rates, u_{ripple} , range from -3.3 m day^{-1} (offshore) to 4.5 m day^{-1} , and 79% of area-averaged migration rates are onshore. The time-mean of u_{ripple} for the entire study period is $1.1 \pm 1.3 \text{ m day}^{-1}$ onshore (the error bar is the standard deviation). In general, there is no significant correlation between the amplitude of the orbital velocity and the migration rate. The largest observed offshore ripple migration rate occurs during the winter of 2002, when larger waves were present at the study site. While we believe that the method confirms that offshore migration does occur, the observations of offshore migration are so infrequent due to sampling limitations that it is difficult to ascribe significance to the offshore rates.

[36] As noted in the introduction, Argus images have been used to determine bathymetry through surface features (i.e., sand bars may be located by surficial patterns of bright intensity due to wave breaking [c.f. *Lippmann and Holman, 1993*]). At Waimea Bay, however, during the weak wave conditions in which the seabed ripples are visible through the water column, the only wave breaking in our study area is at the shoreline. While it is possible to track the shoreline location using Argus images, we do not have sufficient in situ observations of beach slope and hence are unable to assess if and when beach change and sediment transport are occurring during the study period.

[37] Given that we have neither direct measurements of sediment transport nor sufficient survey- or Argus-based estimates of beach profile change during our study period, we can only speculate on the role that ripple migration may play in sediment transport at Waimea. That ripples are observed to migrate does not imply that sand is transported with the migrating pattern. However, in order to assess the

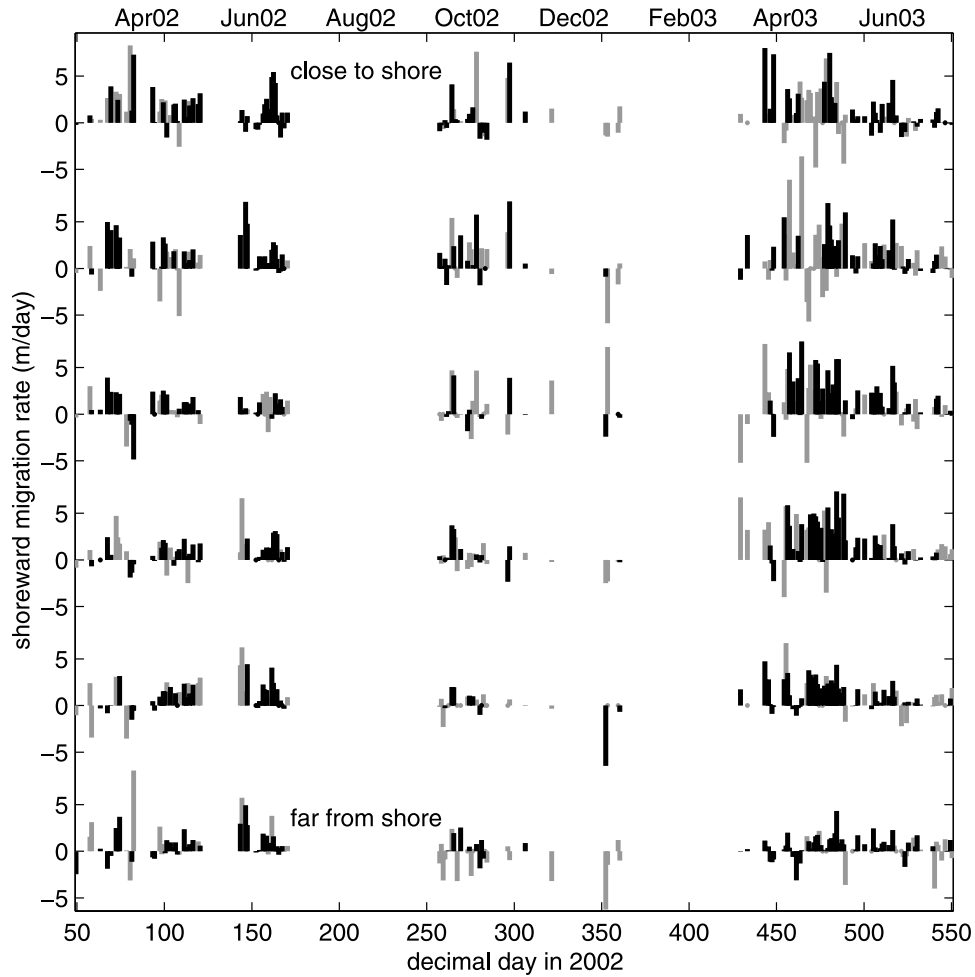


Figure 10. Alongshore averaged ripple velocities in 4-m bins for the six cross shore lines in the white box of Figure 9. Bars are in gray at times when velocities were found for fewer than 40% of the alongshore points in the line. Positive rates are directed onshore.

hypothesis that ripple migration has the potential to transport sand at Waimea, we follow previous migration studies and estimate the sand volume transport rate associated with ripple migration to determine if these transport estimates are of the same order as previous observations of sand transport at Waimea [Dail *et al.*, 2000]. Assuming that the entire volume of sand contained in the ripples is transported with the ripples, the transport may be related to the migration rate according to

$$Q_{ripple} = (1 - \varepsilon)\zeta u_{ripple}, \quad (5)$$

where $\varepsilon = 0.35$ is the porosity [Sleath, 1984], ζ is the ripple height, and u_{ripple} is the rate of ripple migration in m day^{-1} [Traykovski *et al.*, 1999]. As we do not have observations of ripple height from Argus, we take $\zeta = 0.17\lambda$, which is valid for orbital ripples [Wiberg and Harris, 1994] and is consistent with our modeling effort in §3.1 (i.e., the ripples have inferred slopes $m = 0.3-0.4$). Transport from (5) varies from $-0.3 \text{ m}^3 \text{ m}^{-1} \text{ day}^{-1}$ (offshore) to $0.5 \text{ m}^3 \text{ m}^{-1} \text{ day}^{-1}$ (onshore, Figure 12); the time-mean of Q_{ripple} is $\sim 0.09 \pm 0.12 \text{ m}^3 \text{ m}^{-1} \text{ day}^{-1}$ over the study period. While we emphasize that we cannot determine, in this study, that sand

is being transported due to the observed ripple migration, these initial estimates of Q_{ripple} from (5) are consistent in magnitude and direction with previous measurements of beach volume change at Waimea Bay: Dail *et al.* [2000] estimated a peak onshore sediment transport of $4 \text{ m}^3 \text{ m}^{-1} \text{ day}^{-1}$ during accretionary periods during the winter but found that spring-summer fluxes are often $\leq 0.1 \text{ m}^3 \text{ m}^{-1} \text{ day}^{-1}$.

4. Conclusions

[38] We have demonstrated that estimates of seabed ripple wavelengths and ripple migration rates may be obtained remotely from Argus images of Waimea Bay. For the time period analyzed (February 2002 through October 2003), time-averaged Argus images show bedforms without special processing approximately 50% of the time during summer wave conditions (April–October) and approximately 15% of the time during winter wave conditions (November–March). While in situ hydrodynamic observations are not available, offshore buoy data are used as input to the SWAN model to obtain estimates of significant wave orbital diameter at the site of the Argus images. The ripple wavelengths

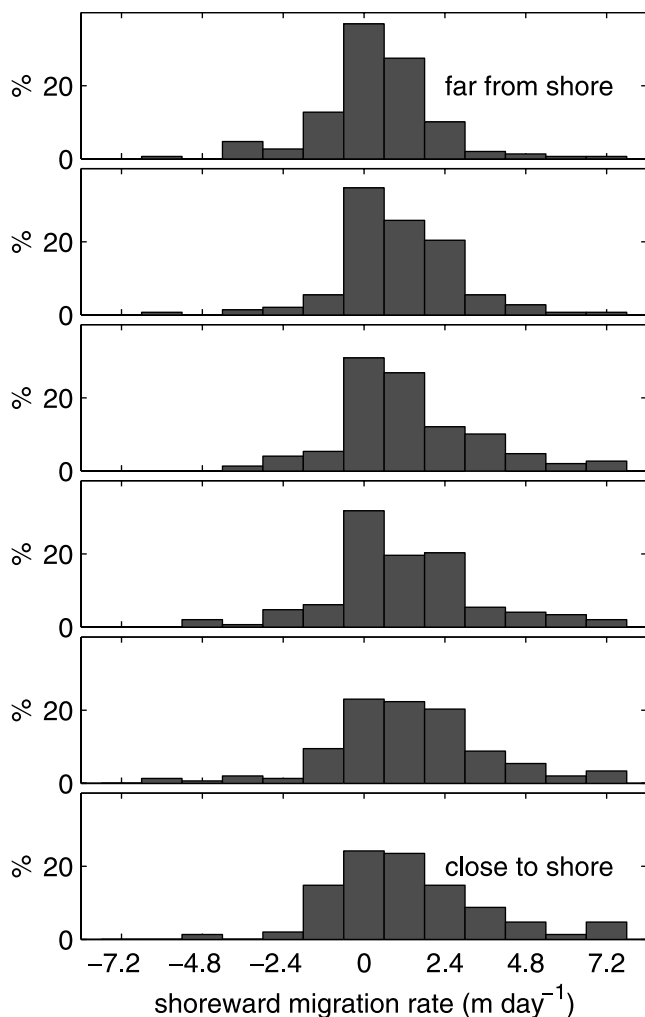


Figure 11. Percent of along-shore averaged ripple migration at each rate for the six cross shore lines (see Figure 9). Positive rates are directed onshore.

determined from the Argus images scale with wave orbital diameter according to $\lambda_p = 0.09d_{0.1/3} + 0.38$ ($R = 0.63$), which differs significantly from observed scalings for orbital ripples (e.g., $\lambda = 0.75d_{0.1/3}$ [Traykovski *et al.*, 1999]). We conclude that our wavelength observations from Argus images largely fall into the suborbital regime and can be described by the suspension-limited model of Smith and Wiberg [2006] as modified by Traykovski [2006], for which the suborbital wavelength is $\lambda_l \propto \frac{w_s T}{m}$, (4). For our wavelength observations, $\lambda_p = 0.06T$ ($R = 0.67$). It appears that the combination of coarse sand and large wave orbital diameters at our shallow study site results in an active ripple field of suborbital wavelengths, rather than one following traditional orbital scalings.

[39] We also have presented observations of ripple migration estimated from lagged correlations between sequential images. Area-averaged migration rates range from -3.3 m day^{-1} (offshore) to 4.5 m day^{-1} , and are onshore 79% of the time (Figure 12). Estimates of sand transport based on the assumption that the entire volume of sand contained in the ripples is transported with the ripples range from $-0.3 \text{ m}^3 \text{ m}^{-1} \text{ day}^{-1}$ (offshore) to $0.5 \text{ m}^3 \text{ m}^{-1} \text{ day}^{-1}$. While our observations are biased toward low-energy wave conditions, ripple migration rates and directions and associated possible sand transport are consistent with the accretion of the beach under low-wave conditions as described by Dail *et al.* [2000]. In general, ripple migration rate and wave orbital velocity estimated from SWAN are not significantly correlated.

[40] We conclude by speculating that ripple migration may be an important mechanism for onshore sand transport during accretionary phases at Waimea Bay. The Argus system provides a means to monitor ripple migration over broad time and space scales. The method could be improved by increased sampling rates and better filtering of surface conditions. In addition, in situ measurements are needed to quantify the hydrodynamic forcing that determines ripple scales and migration rates, to determine the relationship between ripple migration and sand transport at this location, and to verify that beach volume changes are consistent with

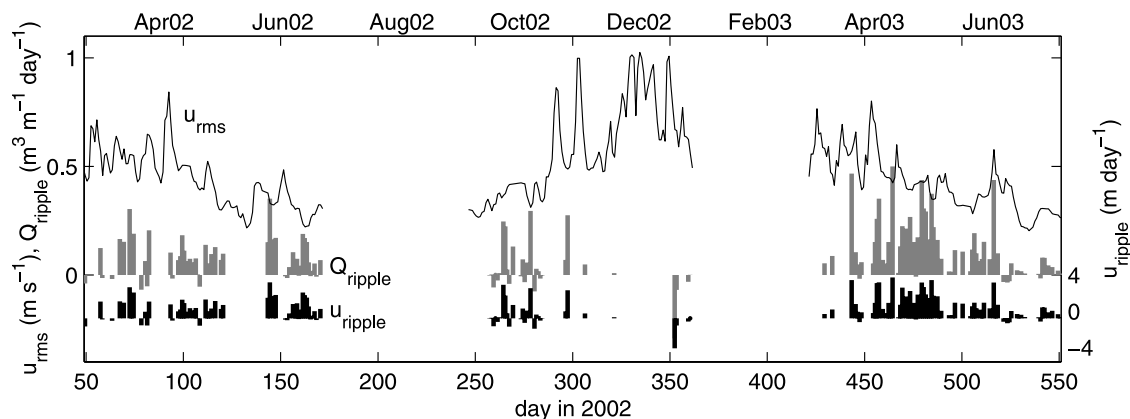


Figure 12. Wave orbital velocity u_{rms} (line), average ripple sediment transport, Q_{ripple} (grey bars), from (5), and average ripple migration rates, u_{ripple} (black bars), over the subgrid (white box in Figure 9). The time-mean of Q_{ripple} is $0.09 \pm 0.12 \text{ m}^3 \text{ m}^{-1} \text{ day}^{-1}$ and of u_{ripple} is $1.1 \pm 1.3 \text{ m day}^{-1}$ over the study period.

the cross-shore sediment transport estimated from ripple migration rates.

Appendix A

[41] The bathymetry, $h(x, y)$, over the image area used in the refraction correction in section 2.2 is estimated from the Argus images as follows. The intensity of light, I , is attenuated in water according to

$$I(r) = I_0 e^{-Kr} \approx I_0(1 - Kr) \quad (\text{A1})$$

where I_0 is the initial intensity, r is the distance traveled, K is the light attenuation coefficient, and we have assumed $Kr \ll 1$. The light intensity measured at the camera, I_M , is the sum of the intensity reflected from the water surface I_{SR} and that reflected from the bottom, I_{BR} :

$$I_M = I_{SR} + I_{BR}. \quad (\text{A2})$$

If I_I is the light intensity incident on the water's surface, $I_T = I_I - I_{SR}$ is the intensity transmitted into the water, and

$$I_{BR} = I_T(1 - Kr), \quad (\text{A3})$$

where

$$r = \frac{2h(x, y)}{\sin \alpha}, \quad (\text{A4})$$

gives the distance traveled by the beam underwater and $\alpha = 42^\circ$ is the angle the light ray makes with the horizontal in the water (we assume α is constant, as it varies by less than 1° over our domain).

[42] Substituting (A3)–(A4) into (A2) and rearranging, we obtain

$$h(x, y) = \frac{I_I - I_M}{I_T} \frac{\sin \alpha}{2K}. \quad (\text{A5})$$

Then, assuming I_I , I_{SR} , and I_T are constant over an image, we find

$$h(x_1, y_1) - h(x_0, y_0) = \frac{I_M(x_0, y_0) - I_M(x_1, y_1)}{I_T} \frac{\sin \alpha}{2K}. \quad (\text{A6})$$

Taking the reference point (x_0, y_0) at the shore where $h(x_0, y_0) = 0$, we obtain

$$h(x, y) \propto I_M(x_0, y_0) - I_M(x, y) \equiv h'(x, y). \quad (\text{A7})$$

where $h'(x, y)$ is the relative depth. We estimate $h'(x, y)$ by averaging five thousand plan view images from the time period analyzed.

[43] The average underwater bed slope at Waimea based on repeat offshore surveys [Dail *et al.*, 2000] is 0.05. From this average slope and a cross-shore distance in the image area of ~ 40 m, the depth range is 0 to 2.2 m from the

shoreline to the seaward extent of the image (Figure 3). We thus scale the relative depth $h'(x, y)$ to obtain

$$h(x, y) = \frac{h'(x, y)}{h'(x_d, y_d)} 2.2, \quad (\text{A8})$$

where (x_d, y_d) is the deepest point (farthest from shore).

[44] This method produces a depth grid ranging from 0.1 to 2.0 m in the analyzed region (Figure 3), with a mean depth of 1.0 m. Although this method is approximate and makes a number of assumptions, the distortions of our image area resulting from refraction correction using an inaccurate depth grid are small.

[45] The data are corrected for refraction according to (1) using the calculated depth grid described above. This correction due to refraction is in the radial direction and varies from 0.11 to 2.16 m across the region analyzed here. The refraction correction in the direction of the average ripple wave vector ranges from 0.05 to 1.32 m. The resulting wavelength stretching, which we are correcting for, is only 3 cm/m. A mean depth error of 1 m in the refraction correction leads to an additional distortion of 1 mm/m in the average wave vector direction, while a factor of two error in the slope leads to an additional distortion of up to 6 cm/m.

[46] Absolute position is important for determining ripple migration. We account for the tide in our refraction correction (1) and note that the maximum tidal water depth change in 1 hour (the time between images used in our ripple migration estimates) is approximately 0.2 m. By comparison between pressure data from a 17-day deployment in 10 m water depth and our tidal predictions, the rms error in hourly water level change is 0.04 m. The resulting cross-shore displacement would be 0.004 m, small compared to the migration rates observed (see Figure 10).

[47] **Acknowledgments.** While this manuscript was in review, P. Traykovski suggested that we compare our ripple observations with the suspension limited model in section 3.1. Discussions with P. Traykovski are greatly appreciated. J. Stanley provided technical advice on the Argus system and data processing. T. Hilmer assisted with the image processing. Discussions with D. Cacchione and S. Elgar also are greatly appreciated. This paper is funded in part by a grant/cooperative agreement from the National Oceanic and Atmospheric Administration, Project R/EP-21, which is sponsored by the University of Hawaii Sea Grant College Program, SOEST, under Institutional grant NA16RG2254 from NOAA Office of Sea Grant, Department of Commerce. The views expressed herein are those of the authors and do not necessarily reflect the views of NOAA or any of its subagencies. UNIH-SEAGRANT-JC-05-06. This work also was funded in part by ONR Coastal Geosciences (N00014-02-1-0154) and the Andrew Mellon Foundation (R.H.). SOEST contribution 6842.

References

- Amos, C. L., A. J. Bowen, D. A. Huntley, J. T. Judge, and M. Z. Li (1999), Ripple migration and sand transport under quasi-orthogonal combined flows on the Scotian Shelf, *J. Coastal Res.*, 15(1), 1–14.
- Ardhuin, F., T. G. Drake, and T. H. C. Herbers (2002), Observations of wave generated vortex ripples on the North Carolina continental shelf, *J. Geophys. Res.*, 107(C10), 3143, doi:10.1029/2001JC000986.
- Booij, N., R. C. Ris, and L. H. Holthuijsen (1999), A third-generation wave model for coastal regions, part I, Model description and validation, *J. Geophys. Res.*, 104(C4), 7649–7666.
- Boyd, R., D. L. Forbes, and D. E. Heffler (1988), Time-sequence observations of wave-formed sand ripples on an ocean shoreface, *Sedimentology*, 35(3), 449–464.
- Clarke, L. B., and B. T. Werner (2003), Synoptic imaging of nearshore bathymetric patterns, *J. Geophys. Res.*, 108(C1), 3005, doi:10.1029/2000JC000780.

- Clifton, H. E., and J. R. Dingler (1984), Wave-formed sedimentary structures: A conceptual model, *Mar. Geol.*, 60(1–4), 165–198.
- Crawford, A. M., and A. E. Hay (2001), Linear transition ripple migration and wave orbital velocity skewness: Observations, *J. Geophys. Res.*, 106(C7), 14,113–14,128.
- Dail, H. J., M. A. Merrifield, and M. Bevis (2000), Steep beach morphology changes due to energetic wave forcing, *Mar. Geol.*, 162(2), 443–458.
- Hanes, D. M., V. Alymov, Y. S. Chang, and C. Jette (2001), Wave-formed sand ripples at Duck, North Carolina, *J. Geophys. Res.*, 106(C10), 22,575–22,592.
- Hasselmann, K., et al. (1973), Measurements of wind-wave growth and swell decay during the Joint North Sea Wave Project (JONSWAP), *Dtsch. Hydrogr. Z.*, 12(A8), suppl., 1–95.
- Holland, K. T., R. A. Holman, T. C. Lippmann, J. Stanley, and N. Plant (1997), Practical use of video imagery in nearshore oceanographic field studies, *IEEE J. Oceanic Eng.*, 22(1), 81–91.
- Holman, R. A., A. H. Sallenger Jr., T. C. Lippmann, and J. Haines (1993), The application of video image processing to the study of nearshore processes, *Oceanography*, 6(3), 78–85.
- Lippmann, T. C., and R. A. Holman (1993), Episodic, non-stationary behavior of two sand bar system at Duck, NC, USA, *J. Coastal Res.*, 5(15), 49–75.
- Miller, M. C., and P. D. Komar (1980), Oscillations and ripples generated by laboratory apparatus, *J. Sediment. Petrol.*, 50(1), 173–182.
- Neilsen, P. (1981), Dynamics and geometry of wave-generated ripples, *J. Geophys. Res.*, 86(C7), 6467–6472.
- Parker, S. (1987), Seasonal changes in beach characteristics on the island of Oahu, Hawaii, M.A. thesis, 122 pp., Dept. of Geogr., Univ. of Hawaii at Manoa, Honolulu.
- Ris, R. C., N. Booij, and L. H. Holthuijsen (1999), A third-generation wave model for coastal regions, part II, Verification, *J. Geophys. Res.*, 104(C4), 7667–7681.
- Sleath, J. F. A. (1984), *Sea Bed Mechanics*, John Wiley, Hoboken, N. J.
- Smith, D. A., and K. F. Cheung (2003), Settling characteristics of calcareous sand, *J. Hydraul. Eng.*, 129(6), 479–483.
- Smith, D. A., and K. F. Cheung (2004), Initiation of motion of calcareous sand, *J. Hydraul. Eng.*, 130(5), 467–472.
- Smith, J. J., and P. L. Wiberg (2006), Ripple geometry in wave-dominated environments, revisited, *Eos Trans. AGU*, 87(36), Ocean. Sci. Meet. Suppl., Abstract OS35D-24.
- Swart, D. H. (1974), Offshore sediment transport and equilibrium beach profiles, *Publ. 131*, Delft Hydrol. Lab., Netherlands.
- Traykovski, P., A. E. Hay, J. D. Irish, and J. F. Lynch (1999), Geometry, migration and evolution of wave orbital ripples at LEO-15, *J. Geophys. Res.*, 104(C1), 1505–1524.
- Wiberg, P. L., and C. K. Harris (1994), Ripple geometry in wave-dominated environments, *J. Geophys. Res.*, 99(C1), 775–789.
- Williams, J. J., and C. P. Rose (2001), Measured and predicted rates of sediment transport in storm conditions, *Mar. Geol.*, 179(1), 121–133.

J. Aucan, Y. L. Firing, and M. Merrifield, Department of Oceanography, University of Hawaii at Manoa, 1000 Pope Road, Marine Sciences Building, Honolulu, HI 96822, USA.

J. M. Becker, Department of Geology and Geophysics, University of Hawaii at Manoa, 1680 East-West Road, POST 813, Honolulu, HI 96822, USA. (jbecker@soest.hawaii.edu)

R. Holman, College of Oceanic and Atmospheric Sciences, Oregon State University, 104 COAS Administration Building, Corvallis, OR 97331-5503, USA.

G. Pawlak, Department of Ocean and Resources Engineering, University of Hawaii at Manoa, 2540 Dole Street, Holmes Hall 402, Honolulu, HI 96822, USA.